Journal of Pharmaceutical Analysis 14 (2024) 100904

Contents lists available at ScienceDirect

Journal of Pharmaceutical Analysis

journal homepage: www.elsevier.com/locate/jpa

Original article

Apatinib and gamabufotalin co-loaded lipid/Prussian blue nanoparticles for synergistic therapy to gastric cancer with metastasis

Binlong Chen [a, b, 1], Yanzhong Zhao [a, *, 1], Zichang Lin [c], Jiahao Liang [d], Jialong Fan [d], Yanyan Huang [a], Leye He [b], Bin Liu [d, **]

[a] Health Management Center, The Third Xiangya Hospital, Central South University, Changsha, 410013, China
[b] Department of Urology, The Third Xiangya Hospital, Central South University, Changsha, 410013, China
[c] Department of Laboratory Medicine, The Third Xiangya Hospital, Central South University, Changsha, 410013, China
[d] College of Biology, Hunan University, Changsha, 410082, China

ARTICLE INFO

Article history:
Received 14 September 2023
Received in revised form
9 November 2023
Accepted 21 November 2023
Available online 29 November 2023

Keywords:
Apatinib
Gamabufotalin
Lipid/Prussian blue nanoparticles
Gastric cancer

ABSTRACT

Due to the non-targeted release and low solubility of anti-gastric cancer agent, apatinib (Apa), a first-line drug with long-term usage in a high dosage often induces multi-drug resistance and causes serious side effects. In order to avoid these drawbacks, lipid-film-coated Prussian blue nanoparticles (PB NPs) with hyaluronan (HA) modification was used for Apa loading to improve its solubility and targeting ability. Furthermore, anti-tumor compound of gamabufotalin (CS-6) was selected as a partner of Apa with reducing dosage for combinational gastric therapy. Thus, HA-Apa-Lip@PB-CS-6 NPs were constructed to synchronously transport the two drugs into tumor tissue. *In vitro* assay indicated that HA-Apa-Lip@PB-CS-6 NPs can synergistically inhibit proliferation and invasion/metastasis of BGC-823 cells via downregulating vascular endothelial growth factor receptor (VEGFR) and matrix metalloproteinase-9 (MMP-9). *In vivo* assay demonstrated strongest anti-tumor growth and liver metastasis of HA-Apa-Lip@PB-CS-6 NPs administration in BGC-823 cells-bearing mice compared with other groups due to the excellent penetration in tumor tissues and outstanding synergistic effects. In summary, we have successfully developed a new nanocomplexes for synchronous Apa/CS-6 delivery and synergistic gastric cancer (GC) therapy.

© 2023 The Authors. Published by Elsevier B.V. on behalf of Xi'an Jiaotong University. This is an open access article under the CC BY-NC-ND license (http://creativecommons.org/licenses/by-nc-nd/4.0/).

1. Introduction

Gastric cancer (GC) is one of the most prevalent digestive system tumors, ranking 5th in terms of incidence and 3rd in mortality [1]. Additionally, 80%–90% of patients diagnosed with advanced GC have already experienced metastasis, resulting in a dismal 5-year survival rate of less than 10% [2,3]. Vascular endothelial growth factor receptors (VEGFRs) have been identified as key mediators of angiogenesis, playing a significant role in the growth and metastasis of GC [4,5]. Apatinib (Apa), a small molecule specifically binds to VEGFR-2 and effectively inhibits tumor development, leading to a reduction in tumor microvascular density [6]. Although Apa has been authorized by the Chinese Food and Drug Administration for the treatment of chemotherapy-resistant advanced GC [7–9], its low bioavailability necessitates a high dosage (750–850 mg/d), which often exacerbates toxic side effects such as hypertension, proteinuria, and hand-foot syndrome [10]. Recently, combination therapies have gained traction in tumor treatment and have shown promising outcomes [11]. Consequently, combining Apa with other drugs could represent an ideal strategy for efficient GC therapy at lower dosages.

Gamabufotalin (CS-6), one kind of compound isolated from famous traditional drug *Chansu*, has been found to possess potent anti-tumor activity at low concentrations, without inducing multi-drug resistance [12,13]. In previous study, we have demonstrated that CS-6 could inhibit distant tumor metastases by significantly downregulating the levels of vascular endothelial growth factor (VEGF) and matrix metalloproteinase-9 (MMP-9) in triple-negative breast cancer (TNBC) [14]. In addition, CS-6 has demonstrated its inhibitory effects on the growth of human glioblastoma cells (U-87) through the downregulation of proteins such as aurora B, cdc25A, cdc25C, cdc2, and cyclin B1, while concurrently upregulating p21 levels [15]. In an additional study, Tang et al. [12] revealed that CS-6 could inhibit angiogenesis of lung cancer cells (A549) by downregulating the levels of VEGF in vascular endothelial cells. Considering the characteristics of rapid growth and propensity for metastasis in advanced GC [16,17], it is reasonable to speculate that a combination of CS-6 and Apa could

* Corresponding author.
** Corresponding author.
E-mail addresses: yanzhongzhao@163.com (Y. Zhao), binliu2001@hotmail.com (B. Liu).
[1] Both authors contributed equally to this work.

https://doi.org/10.1016/j.jpha.2023.11.011
2095-1779/© 2023 The Authors. Published by Elsevier B.V. on behalf of Xi'an Jiaotong University. This is an open access article under the CC BY-NC-ND license (http://creativecommons.org/licenses/by-nc-nd/4.0/).

serve as an alternative strategy for GC therapy by effectively inhibiting tumor growth and metastasis.

However, the low hydrophilicity and bioavailability of Apa and CS-6 often result in low efficacy *in vivo*. Additionally, another challenge is how to deliver both Apa and CS-6 simultaneously to the tumor, considering their different pharmacological characteristics. In recent years, nanomaterials-based drug delivery systems (DDS) with high solubility and tumor targeting ability provided the strong weapon for dissolving these drawbacks. For example, some studies have developed several kinds of hydrogel based DDS for efficient GC therapy [18–21] (Table S1). However, this kind of nanomaterials are limited to *in-situ* therapy. On the other hand, Prussian blue nanoparticles (PB NPs), another type of nanomaterials with clinical application permitted by U.S. Food and Drug Administration showed excellent stability and biocompatibility for *in vivo* administration [22]. In our previous studies, PB NPs have successfully delivered various drugs, such as shikonin, artemisinin, procyanidins, and silver nanoparticles for the treatment of different diseases [23–26]. Nevertheless, the hydrophobic nature of Apa results in low loading efficiency onto PB NPs. To address this issue and enable co-loading of CS-6 and Apa, we prepared a novel lipid bilayer coated PB NPs system. Initially, we synthesized Apa-Lip according to the method proposed by Sackmann et al. [27]. Subsequently, PB-CS-6 NPs were added to the surface of lipid film (containing Apa-Lip) for hydration. This process allowed us to obtain the lipid-film-coated PB NPs with loaded Apa and CS-6. Considering the high expression of CD44 on the GC cells [28], hyaluronan (HA) was adopted to enhance the tumor-specific accumulation of nanodrug through the interaction between HA and CD44. The pH-sensitive 1, 2-distearoyl-sn-glycero-3-phosphoethanolamine-poly (2-ethyl-2-oxazoline) (DSPE-PEOz) in the lipid film could efficiently control the release of Apa under tumor acidic environments to realize synergistic GC therapy with CS-6 (Scheme 1).

2. Materials and methods

2.1. Materials

Apa was acquired from Shanghai Macklin Biochemical Co., Ltd (Shanghai, China). CS-6 was purchased from Herbest (Xi'an, China). DSPE-PEOz2K was obtained from Xi'an RuiXi Biological Technology Co., Ltd (Xi'an, China). $FeCl_3 \cdot 6H_2O$ was obtained from Shanghai Aladdin Biochemical Technology Co., Ltd (Shanghai, China). $K_4[Fe(CN)_6] \cdot 3H_2O$ was purchased from Tianjin Guangfu Fine Chemical Research Institute (Tianjin, China). Lecithin and cholesterol were purchased from Shanghai Ryon Biological Technology Co., Ltd (Shanghai, China). N-hydroxysuccinimde (NHS), 1,2-dichloroethane (EDC), and dimethyl sulfoxide (DMSO) were purchased from Sigma-Aldrich (St. Louis, MO, USA). Chlorine6 (Ce6) was purchased from Shanghai Yuanye Bio-Technology Co., Ltd (Shanghai, China). MMP-9, cyclin D1 and β-actin antibodies were purchased from Proteintech (Rosemont, IL, USA). VEGF was obtained from Beyotime (Shanghai, China).

2.2. Cell lines and animals

BGC-823 cells, H9C2 cells, and human umbilical vein endothelial cells (HUVECs) were provided by Xiangya Central Laboratory,

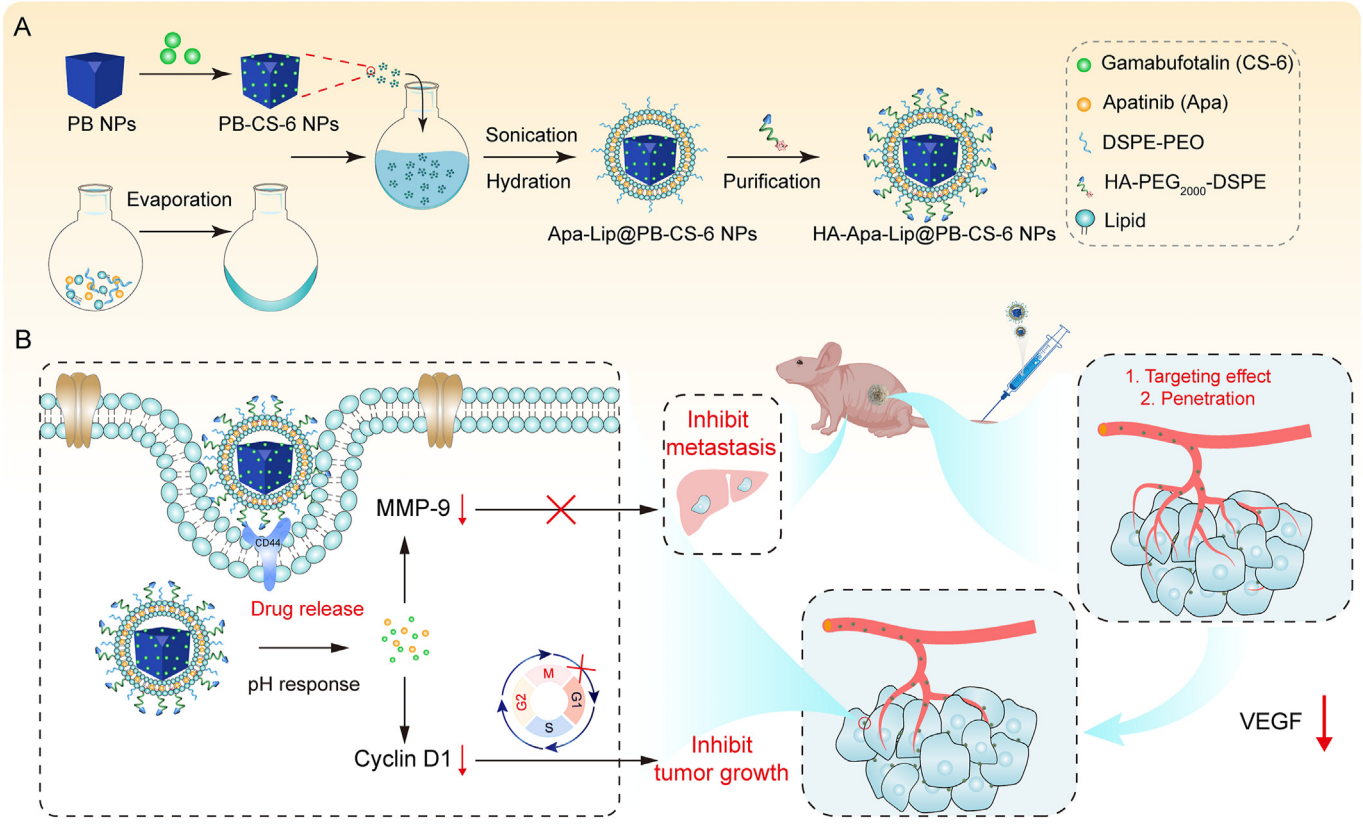

Scheme 1. (A) The synthetic process of hyaluronan-apatinib-Lip@Prussian blue-gamabufotalin nanoparticles (HA-Apa-Lip@PB-CS-6 NPs). (B) Proposed mechanism of HA-Apa-Lip@PB-CS-6 NPs mediated proliferation inhibition and metastasis inhibition in BGC-823 cells. DSPE-PEO: 1, 2-distearoyl-sn-glycero-3-phosphoethanolamine-poly (2-ethyl-2-oxazoline); HA-PEG_{2000}-DSPE: hyaluronan-polyethylene glycol $_{2000}$-1, 2-distearoyl-sn-glycero-3-phosphoethanolamine; MMP-9: matrix metalloproteinase-9; VEGF: vascular endothelial growth factor.

Central South University. All cells were cultured in Dulbecco's modified eagle medium (DMEM) (Logan, UT, USA) supplemented with 10% fetal bovine serum (FBS) (Lonsera, Nanjing, China) and 1% penicillin-streptomycin (PS) (Invitrogen, Carlsbad, CA, USA). Female BALB/c nude mice were provided by Hunan SJA Laboratory Animal Co., Ltd. All experiments involving animals conformed to the guiding principles of the "Declaration of Helsinki" and have been approved by the Medical Ethics Committee of Hunan University (Approval number: SYXK-2018-0006).

2.3. Synergistic anti-tumor effects of Apa and CS-6 at different combination ratios in vitro

BGC-823 cells were seeded in 96-well plates at a density of 8×10^3 cells per well. The cells were treated with different ratios of Apa and CS-6 in each well (Apa: 0, 5, 10, 15, and 20 μM; CS-6: 0, 15, 30, 45, and 60 nM). 48 h later, the cell viability was determined using the following formula:

$$\text{Cell viability } (\%) = \frac{(\text{OD})_{490\text{nm/sample}}}{(\text{OD})_{490\text{nm/control}}} \times 100\%$$

The SynergyFinder software was used to calculate the synergistic effect of the Apa and CS-6, with values less than −10 indicating antagonism, values between −10 and 10 indicating a combined effect, and values greater than 10 indicating synergy [29]. GraphPad Prism software was used for data presentation.

2.4. Synthesis of HA-Apa-Lip@PB-CS-6 NPs

2.4.1. Synthesis of PB-CS-6 NPs

For the preparation of A solution, 0.0541 g of $FeCl_3 \cdot 6H_2O$ was dissolved in 2 mL of water, and then 200 μL of this solution was diluted to 20 mL with citric acid solution (25 mM) to obtain 1 mM $FeCl_3$ solution. Then the resulting solution was dissolved with magnetic stirring and heated to 60 °C under a water bath. For the preparation of B solution, 0.0085 g of $K_4[Fe(CN)_6] \cdot 3H_2O$ was dissolved in 20 mL of citric acid solution (25 mM) to realize the solution with concentration of 1 mM $K_4[Fe(CN)_6]$. Similar to solution A, solution B was dissolved with magnetic stirring and heated to 60 °C using a water bath. Subsequently, 20 mL of heated solution B was added dropwise into 20 mL of solution A under magnetic stirring in the water bath maintained at 60 °C. This reaction mixture underwent a color change process of "light yellow-turquoise-light blue-pure blue". The resulting solution was continuously stirred for 30 min under the water bath at 60 °C. After cooling to 25 °C, carboxylated PB NPs solution was centrifuged at 15,000 rpm. The obtained precipitate was washed 3 times with ultrapure water, and finally, the purified nanoparticles were lyophilized by freeze-drying method, and the freeze-dried nanoparticles were stored at −20 °C. To prepare PB-CS-6 NPs, 200 μL of PB water solution (5 mg/mL) was added to 800 μL DMSO solution containing 100 μg CS-6, and continuously stirred for 6 h at room temperature. After centrifugation at 15,000 rpm for 20 min, PB-CS-6 NPs were obtained.

2.4.2. Synthesis of Apa-Lip@PB-CS-6 NPs

Based on previous literature [30], we screened a combination of lecithin/cholesterol/DSPE-PEOz/Apa in a mass ratio of 8:1:2:2, which can obtain stable and uniform lipid film. Briefly, lipid film was achieved in a round-bottom flask after evaporation by using a rotary evaporator at 37 °C. Then, the 5 mL aqueous solution of PB-CS-6 was added on the surface of lipid film for 1 h hydration after sonication for 1 min (20 W, 0.5/0.5 s on/off). Following 1 h hydration, there was 1 min sonication (20 W, 0.5/0.5 s on/off) to sonicate above particle suspension. Since the suspension contained coated particles (Apa-Lip@PB-CS-6), liposomes, and free drug, the Apa-Lip@PB-CS-6 NPs were separated and purified by centrifugation at 15,000 rpm for 30 min at room temperature, followed by washing for 3 times in double distilled water.

2.4.3. Synthesis of HA-Apa-Lip@PB-CS-6 NPs

HA-PEG_{2000}-DSPE was prepared according to our previous method [31]. Briefly, HA-PEG_{2000}-DSPE was inserted into the lipid film of Apa-Lip@PB-CS-6 NPs to achieve HA-Apa-Lip@PB-CS-6 NPs.

2.4.4. Synthesis of PB^{Ce6} NPs

Briefly, 5 mL of Ce6 DMSO solution (5 mg/mL) with activated carboxyl group were mixed with 5 mL PB NPs water solution (5 mg/mL) and the mixture was continuously stirred at 800 rpm for 24 h in the dark to obtain PB^{Ce6} NPs. The PB^{Ce6} NPs solution was used for synthesize of HA-Lip@PB^{Ce6} and Lip@PB^{Ce6} according to above methods.

2.5. Controlled release of Apa and CS-6 from HA-Apa-Lip@CS-6 NPs

To determine the drug release behavior from HA-Apa-Lip@CS-6 NPs, 2 mL of nanoparticles solution (with equivalent loaded Apa or CS-6) was dialyzed in phosphate buffered saline (PBS) with pH 5.2, pH 6.5 or pH 7.4 by stirring in the water bath at 37 °C (MWCO = 2.5 kDa). The amount of Apa or CS-6 in different solutions (PBS at pH 5.2, pH 6.5, or pH 7.4) at specified point of time (2, 4, 6, 8, 12, 24, 36, 48, 60, 72, 96, and 120 h) were detected by UV-Vis spectrophotometer (Beckman Coulter, Inc., BREA, CA, USA), and PBS with pH 5.2, pH 6.5 or pH 7.4 was added at different time point mentioned above to keep the constant volume.

2.6. Biocompatibility analysis

The cytotoxicity of nanoparticles on BGC-823 cells, HUVECs, and H9C2 cells was evaluated by 3-(4,5-dimethylthiazol-2-yl)-2,5-diphenyltetrazolium bromide (MTT) assay. Briefly, after culture for 24 h, each well of 96-well plates (5×10^3 cell/well) was treated with 12.5, 25, 50, and 100 μg/mL HA-Lip@PB NPs for another 24 h, respectively.

The hemolysis assay was conducted according to our previous methods [32]. Briefly, 4% red blood cells (RBCs) suspension was incubated with water (positive control), PBS (negative control), and HA-Apa-Lip@PB-CS-6 NPs at different concentration. After 6 h incubation in cell incubator, the supernatants of all sample were collected after centrifugation. Subsequently, the OD_{562nm} of above supernatant was measured for evaluating hemolysis rate. Besides, the morphological images of erythrocytes were captured under microscopes.

According to previous experimental methods [33], we carried out platelet aggregation assay. In brief, plasma from BALB/c mice mingled with thrombin, PBS, PB-CS-6 NPs and HA-Apa-Lip@PB-CS-6 NPs (100 μg/mL), respectively, and then above mixture was incubated in a thermostatic incubator (37 °C) for 1 h before OD_{650nm} was measured.

2.7. Cell uptake and penetrating ability assay

The BGC-823 cells seeded into confocal dishes (5×10^4 cells/well) of a 12-well plate were cultured with HA-Lip@PB^{Ce6} and Lip@PB^{Ce6} (the concentration of Ce6 was 5 μg/mL in each group) for 2−6 h. After stained by Hoechst 33342, cell images were recorded by using confocal laser scanning microscope (CLSM). In the control experiment, the HA was added into wells in advance and incubated for 1 h in HA pretreatment group. Then, cells were incubated with PBS, free Ce6, Lip@PB^{Ce6}, HA-Lip@PB^{Ce6} and HA-Lip@PB^{Ce6} (HA pretreatment group) for 4 h.

2.7.1. In vitro deep penetration study

To gain the multicellular spheroids (MCSs), the cell mixture containing 2.5% Matrigel (Corning Matrigel Matrix, Tewksbury, MA, USA) was seeded into wells coated with agarose (5×10^3 cells/well). After 10 days, the formed MCSs were treated with free Ce6, HA-Lip@PB^{Ce6} NPs (5 μg/mL Ce6) for 12 h. Finally, the fluorescence images of different depth of MCSs were captured by CLSM and the software of Image J was used for fluorescence intensities analysis.

2.8. In vitro assessment of anticancer activity

2.8.1. Cell viability assay

After culture for 24 h, BGC-823 cells (8×10^3 cells/well) seeded in a 96-well plate were treated with PBS, Apa (20 μM), CS-6 (30 nM), Apa&CS-6 (Apa: 20 μM, CS-6: 30 nM) and HA-Apa@PB-CS-6 NPs (containing 20 μM of Apa and 30 nM of CS-6) for 48 h incubation, and the cell viability was calculated using MTT assay.

2.8.2. Cell cycle analysis

After cultivation for 24 h, BGC-823 cells (1×10^5 cells/well) seeded in the 6-well plate were treated with PBS, Apa (20 μM), CS-6 (30 nM), Apa&CS-6 (Apa: 20 μM, CS-6: 30 nM) and HA-Apa@PB-CS-6 NPs (containing 20 μM of Apa and 30 nM of CS-6). 48 h later, harvested cells were fixed with ethanol for another 24 h at 4 °C and then all cells stained by the cell cycle detection kit (Beyotime, Shanghai, China). Data of cell cycle was analyzed by flow cytometry (Cytek Athena, Los Angeles, CA, USA).

2.8.3. Cell proliferation assay

This assay was performed by using an 5-ethynyl-2'-deoxyuridine (EdU) kit (Beyotime, Shanghai, China). Briefly, BGC-823 cells (2×10^4 cells/well) seeded in the 24-well plate were cultured with different formulations (PBS, Apa, CS-6, Apa&CS-6 and HA-Apa-Lip@PB-CS-6 NPs) for 44 h. Next, all cells were incubated with EdU for another 4 h, fixed with 4% paraformaldehyde for 20 min, and permeated with 0.3% Triton X-100 for 15 min. After incubation with the click reaction mixture and Hoechst 33342, cell images were recorded using CLSM.

2.8.4. Colony formation assay

BGC-823 cells (1×10^3 cells/well) seeded in the 6-well plate were treated with various formulations (PBS, Apa, CS-6, Apa&CS-6 and HA-Apa-Lip@PB-CS-6 NPs). Seven days later, the colonies were dyed with 0.2% crystal violet and the images were captured by microscope after having washed with PBS.

2.8.5. Western blotting analysis

The BGC-823 cells were incubated with PBS, Apa, CS-6, Apa&CS-6 and HA-Apa-Lip@PB-CS-6 NPs (containing the same concentration of Apa/CS-6) for 48 h. The whole proteins of each well were extracted. Next, the protein concentration was detected, and the expression of related proteins (β-actin, VEGF, MMP-9, and cyclin D1) was detected by Western blotting.

2.9. Cell migration/invasion assays

2.9.1. Wound healing assay

According to our previous experimental methods [14], when the monolayer cells of BGC-823 filled the entire well, a sterile pipette tip was used to scratch cells and the cells were washed with PBS. Subsequently, PBS, Apa, CS-6, Apa&CS-6 and HA-Apa-Lip@PB-CS-6 NPs were added. 48 h later, the images of the scratch areas were recorded using microscope (OLYMPUS, Tokyo, Japan).

2.9.2. Transwell assay

Briefly, the BGC-823 cells were incubated with PBS, Apa, CS-6, Apa&CS-6 and HA-Apa-Lip@PB-CS-6 NPs in the 6-well plates. 48 h later, Cells in each well were collected for preparing cell suspension and FBS-free DMEM (containing 5×10^4 cells from cells suspension) was added to the upper chamber of the inserts. To investigate cell invasion ability, the transwell-membrane was covered with 10% matrigel (30 μL). After culturing for 24 h (migration assays) or 48 h (invasion assay), the cells were stained with crystal violet solution for 20 min. Finally, images of cells in each well were recorded under a microscope (OLYMPUS, Tokyo, Japan).

2.10. In vivo distribution studies of nanoparticles

2.10.1. Tumor targeting and biodistribution assay

When the tumor volume of BGC-823 tumor-bearing nude mice reached about 200 mm^3, 200 μL of Lip@PB^{Ce6}and HA-Lip@PB^{Ce6} NPs (with an equivalent amount of 5 mg/kg Ce6) were respectively administered intravenously to the mice. After administration, the BGC-823 tumor-bearing nude mice were photographed at different time points with the interactive video information system (IVIS) kinetics optical system (PerkinElmer, Waltham, MA, USA). The BGC-823 tumor-bearing nude mice were sacrificed at 48 h, and all the tumor tissues and major organs (heart, liver, spleen, lung, and kidney) were collected to obtain fluorescence images.

2.10.2. Penetrating ability study in vivo

To determine penetrating ability of HA modified nanoparticles in tumor site. Tumors mentioned above were made into frozen sections, which were stained with 4',6-diamidino-2-phenylindole (DAPI) (Sigma-Aldrich, St. Louis, MO, USA) before CLSM imaging.

2.10.3. Blood circulation time study

Ce6 and HA-Lip@PB^{Ce6} NPs (containing 2.5 mg/kg Ce6) were intravenously injected into normal BALB/c mice, respectively. Next, 100 μL of blood sample was collected from mice in each group at setting time points (0.5–12 h) and analyzed using the IVIS for fluorescence images and fluorescence intensity analysis.

2.11. In vivo anti-tumor activity assay

When tumor volumes of heterotopic BGC-823 tumor-bearing nude mice reached 100 mm^3, these BGC-823 tumor-bearing nude mice were randomly divided into 5 groups (5 mice per group): I) intravenous injection of PBS, II) intravenous injection of Apa, III) intravenous injection of CS-6, IV) intravenous injection of Apa&CS-6, V) intravenous injection of HA-Apa-Lip@PB-CS-6 NPs (Apa: 5 mg/kg; CS-6: 1 mg/kg), meanwhile, healthy mice were used as the normal group. Measurement of tumor volume and body weight were at 2 days interval.

After morphological observations, tumor tissues and major organs were photographed and collected as soon as mice were sacrificed. These tumors tissues and major organs were stained for immunofluorescence or immunohistochemistry tests (hematoxylin and eosin (H&E), Ki67, MMP-9, and VEGF staining). Moreover, the metastatic nodules of liver tissue and weights of spleens were recorded in each group. Meanwhile, fresh blood samples of mice in each group were collected for hematological and biochemical analysis.

2.12. Statistical analysis

Error bars in each figure were expressed as the mean ± standard deviation (SD) and performed at least 3 times. Comparative analysis of the difference between groups was calculated by one-way

analysis of variance (ANOVA) with GraphPad Prism 8.4.0. A significant difference was defined as $^{*}P < 0.05$, $^{**}P < 0.01$, and $^{***}P < 0.001$.

3. Results and discussion

3.1. Assessment of synergistic effect of Apa and CS-6 on gastric cancer cells

To maintain the anti-tumor efficacy of CS-6 on GC while minimizing cardiotoxicity, we implemented a combination approach involving Apa/CS-6. Although CS-6 has showed significant anti-tumor potential in breast cancer and GC, its clinical application is hindered by its potential for cardiotoxicity at high concentrations [34,35]. Initially, we investigated the cytotoxic activity of Apa and CS-6 on BGC-823 cells. Both compounds demonstrated dose-dependent killing of GC cells, with IC_{50} values of 44.20 μM and 50.37 nM, respectively (Fig. 1A). Subsequently, we examined the impact of Apa and CS-6 on BGC-823 cells individually. At concentrations of 20 μM and 30 nM, respectively, Apa and CS-6 resulted in cell viabilities of 97.7% and 72.3%, respectively (Fig. 1B). Conversely, the combination of 20 μM Apa and 30 nM CS-6 reduced the cell viability of BGC-823 cells to 51.3%. Importantly, by calculating the synergistic score of ratios, we found that Apa/CS-6 with 20 μM/30 nM exhibited the highest synergistic score of 22.4 (Fig. 1C). A score above 10 indicated the presence of a synergistic effect between the two drugs [29].

3.2. Characterization of HA-Apa-Lip@PB-CS-6 NPs

The synthesis procedure of HA-Apa-Lip@PB-CS-6 NPs and the proposed anti-tumor mechanism of the combinational strategy are schematically depicted in Scheme 1. In Figs. 2A and B, transmission electron microscope (TEM) and scanning electron microscope (SEM) images displayed the cubic morphology of PB NPs and HA-Apa-Lip@PB-CS-6 NPs, respectively. The average size of the NPs was approximately 89.4 nm and 101.5 nm as shown in Fig. 2C. Furthermore, the color of PB NPs solution was different from that of HA-Apa-Lip@PB-CS-6 NPs (Fig. 2D). Upon loading CS-6, surface zeta potential of PB NPs varied from −21.8 mV to −28.2 mV. After the lipid-film coating and HA modification, the surface zeta potential of PB-CS-6 NPs decreased to −47 mV (Fig. 2E). UV-Vis spectra in Fig. 2F indicated that the characteristic peaks of Apa, CS-6 and PB were at 340 nm, 300 nm, and 710 nm, respectively. Meanwhile, the characteristic peak of Apa at 340–360 nm also appeared in the HA-Apa-Lip@PB-CS-6 NPs. Fourier-transform infrared (FT-IR) spectra further confirmed drugs loading in HA-Apa-Lip@PB-CS-6 NPs. FT-IR

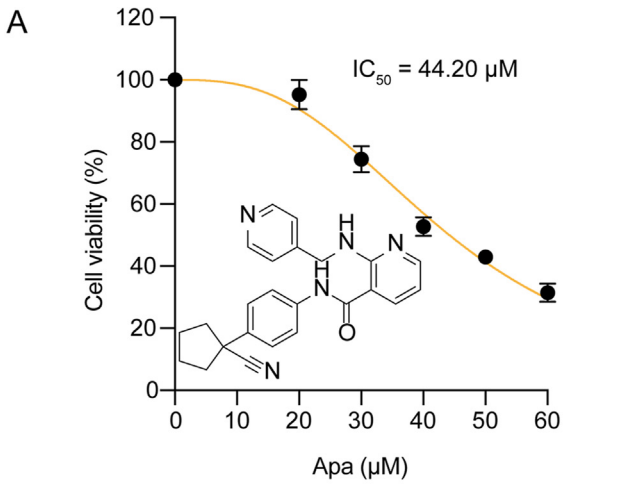

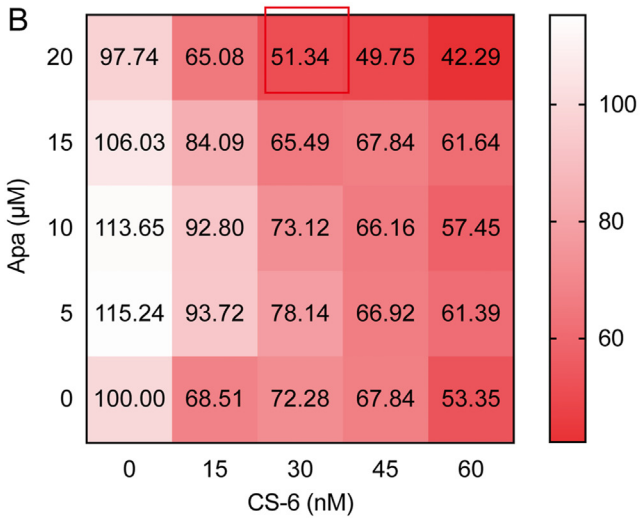

C

Synergy scores of free Apa/CS-6 concentration in mixtures

Apa (μm)	20	25	15	20	5	10	20	20
CS-6 (nm)	15	15	30	30	45	45	45	60
Synergy scores	3.7	10.8	7.3	22.4	1.0	1.8	19.4	11.8

Fig. 1. Assessment of synergistic effect of apatinib (Apa) and gamabufotalin (CS-6). (A) Chemical structure of Apa and CS-6 and their IC_{50} values on BGC-823 cells for 48 h. (B) Series of Apa/CS-6 combinations at different ratios were prepared to detect cell viability. (C) Synergy scores calculated by SynergyFinder software were used to evaluate the synergistic effect of free Apa/CS-6 at different ratios. Bars represented means ± standard deviation (SD) ($n = 3$).

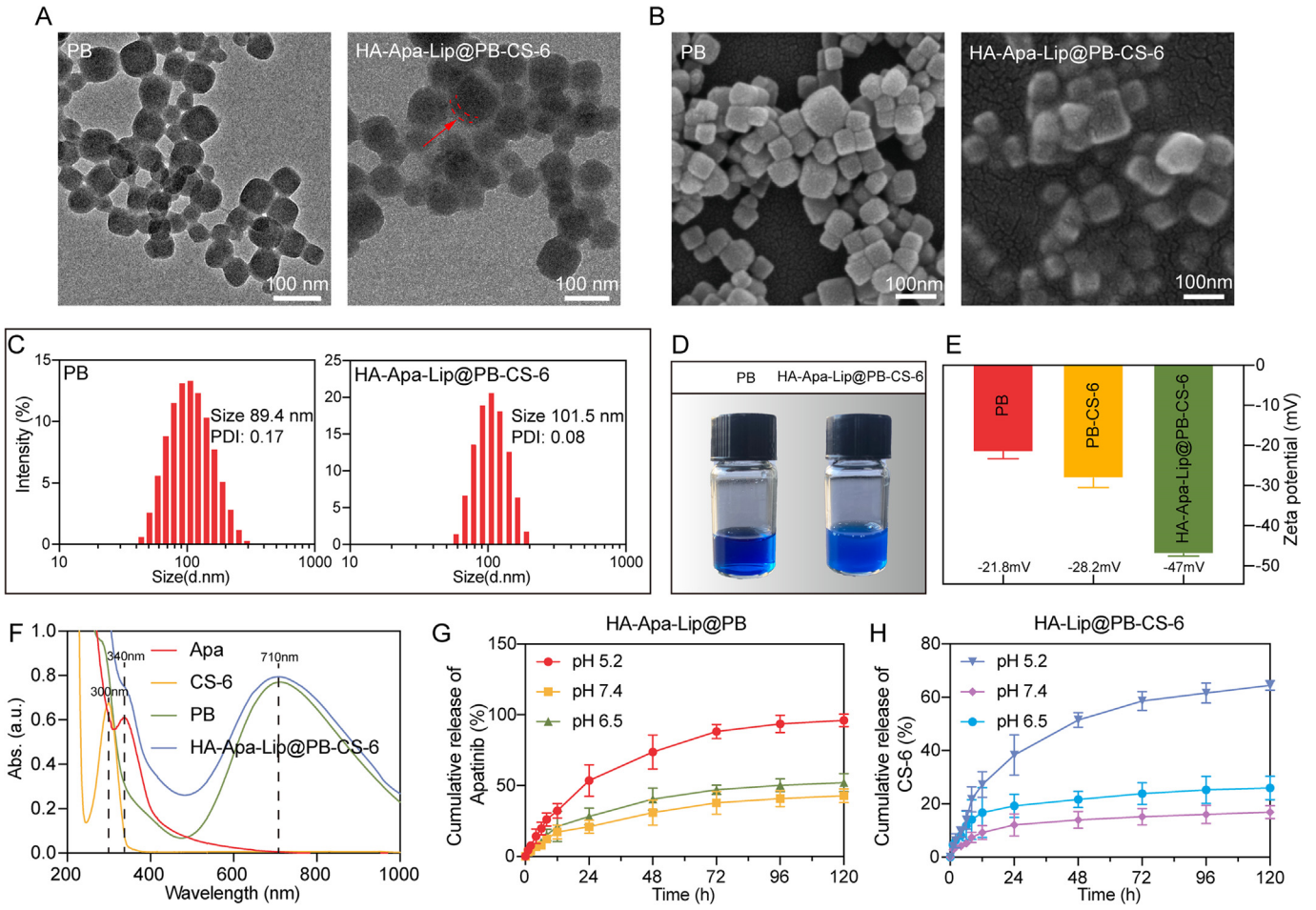

Fig. 2. Characterization of the hyaluronan-apatinib-Lip@Prussian blue-gamabufotalin nanoparticles (HA-Apa-Lip@PB-CS-6 NPs). (A, B) Transmission electron microscope (TEM) images and scanning electron microscope (SEM) images of PB NPs and HA-Apa-Lip@PB-CS-6 NPs. (C) Size distribution of PB NPs (89.4 nm, PDI: 0.17) and HA-Apa-Lip@PB-CS-6 NPs (101.5 nm, PDI: 0.08). (D) The color of PB NPs and HA-Apa-Lip@PB-CS-6 NPs solution. (E) Zeta potentials of PB (−21.8 mV), PB-CS-6 (−28.2 mV) and HA-Apa-Lip@PB-CS-6 NPs (−47 mV). (F) UV-Vis spectra of Apa, CS-6, PB NPs and HA-Apa-Lip@PB-CS-6 NPs. (G, H) Release behavior of Apa (G) and CS-6 (H) from nanoparticles at different pH buffer solutions (pH 5.2, pH 6.5, and pH 7.4). PDI: polymer dispersity index.

revealed −OH peak (3400 cm^{-1}) in PB NPs and C≡N (2210 cm^{-1}) peak of CS-6 with enhanced amplitude and Apa (C═O: 1740 cm^{-1}, δ_{CH}: 915 cm^{-1}) in HA-Apa-Lip@PB-CS-6 NPs (Fig. S1). By optimizing the mass ratio of lecithin/cholesterol/DSPE-PEOz/Apa, we found the entrapment efficiency of Apa was 90.4% at the ratio 8:1:2:2. Meanwhile, the loading efficiency of 1.8% for CS-6 was found under the ratio of CS-6/PB with 1:10 (Fig. S2). These optimal ratios confirmed the synergistic ratio of drugs in nanocarrier. By observing the stability of HA-Apa-Lip@PB-CS-6 NPs in different buffers (H_2O, PBS and DMEM buffer) for 15 days, no change was found in these samples, which demonstrated the long-term stability of this kind of nanodrug under complicated condition (Fig. S3). Considering the tumor acidic endosome/lysosome environment (pH 4.5−pH 5.5) [36], we investigated the effect of pH value on the drug release of HA-Apa-Lip@PB-CS-6 NPs.As shown in Figs. 2G and H, the drug release rate reached 96.1% for Apa and 64.4% for CS-6 after incubation under acidic condition (pH 5.2) for 120 h, while only 42.8% and 17.0% of the loaded Apa and CS-6 were released from NPs under pH 7.4 condition, and there were only 52.1% of the loaded Apa and 26.0% of loaded CS-6 were released from NPs under pH 6.5 condition. This result, which was consistent with previous study [37], demonstrated the incorporation of pH-sensitive lipid DSPE-PEOz successfully facilitated the release of Apa and CS-6 in the endosomes/lysosomes within tumor cells. Additionally, 48 h later, the drug release ratio aligned with the synergistic ratio of two-drug combination under pH 5.4 condition. Therefore, the drug release behavior suggested the generation of synergistic effect of the two drugs, when the HA-Apa-Lip@PB-CS-6 NPs were used for tumor treatment.

3.3. Biocompatibility of HA-Apa-Lip@PB-CS-6 NPs

Both of PB NPs and liposome are United States Food and Drug Administration (US FDA)-approved components known for their high safety [22,38]. In this study, we also demonstrated the biocompatibility of HA-Apa-Lip@PB-CS-6 NPs. After a 48 h incubation period with BGC-823 cells, HUVECs, and H9C2 cells for 48 h, the cell viability of all cell lines was over 80.0%, even at the high concentration of HA-Lip@PB NPs (equivalent to 100 μg/mL PB NPs), which indicated the low cytotoxicity of the nanoparticles on them, including cardiomyocytes (Fig. 3A). To assess the potential toxicity of the drugs on cells, HUVECs and H9C2 cells were cultured with PB NPs, Apa, CS-6 and HA-Apa-Lip@PB-CS-6 NPs. The high cell viability in Fig. S4 furtherly indicated splendid biocompatibility of these materials. Coagulation assay demonstrated a lower risk of platelet aggregation in PBS, PB-CS-6, and HA-Apa-Lip@PB-CS-6 NPs treated whole blood, compared with the positive group receiving thrombin treatment (Fig. 3B). Additionally, the hemolysis rate of

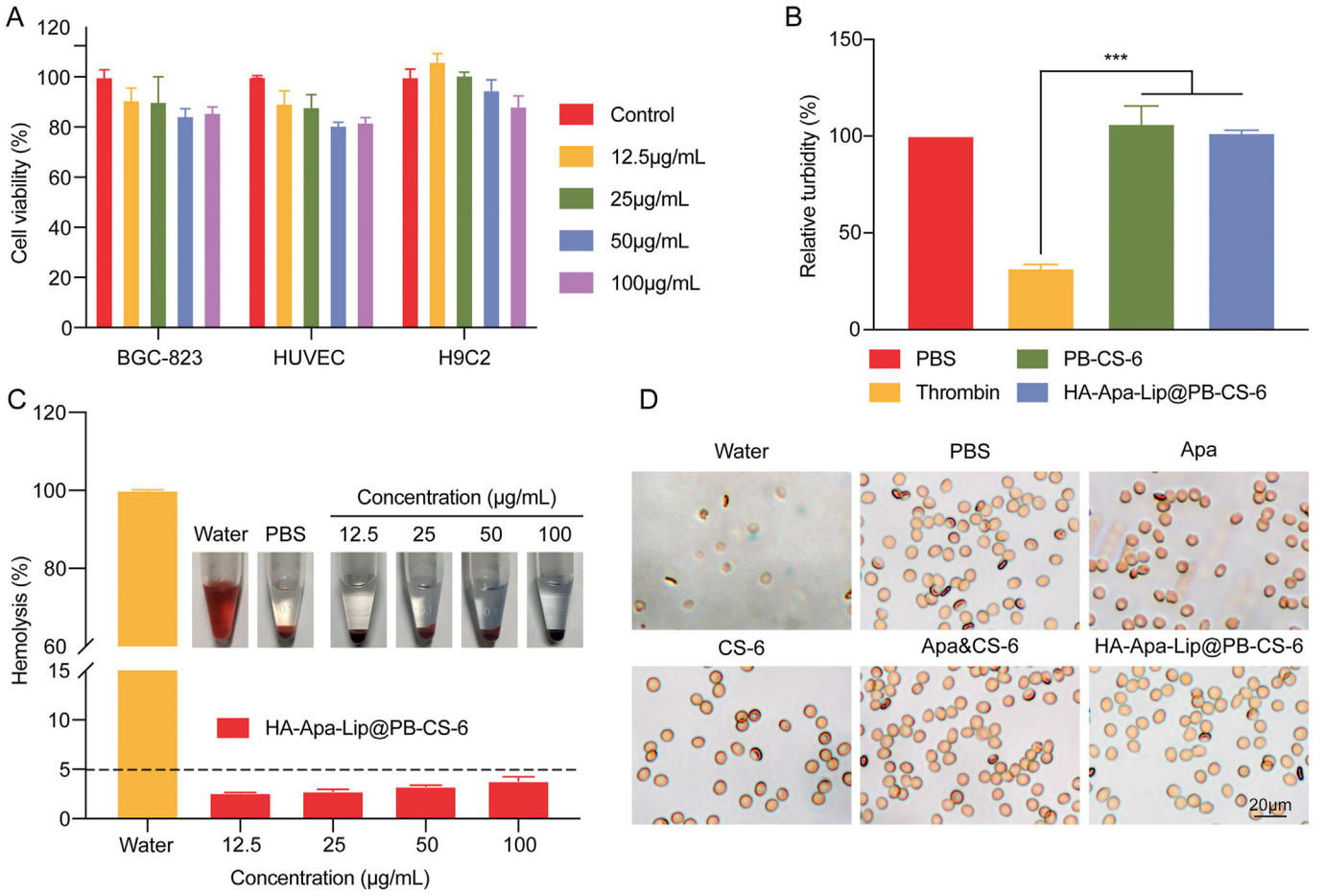

Fig. 3. Biocompatibility of hyaluronan-apatinib-Lip@Prussian blue-gamabufotalin nanoparticles (HA-Apa-Lip@PB-CS-6 NPs). (A) Cytotoxicity of HA-Lip@PB NPs to BGC-823 cells, human umbilical vein endothelial cells (HUVECs), and H9C2 cells. (B) Blood coagulation quantification of phosphate buffered saline (PBS), thrombin, PB-CS-6 NPs, and HA-Apa-Lip@PB-CS-6 NPs. (C) Hemolysis research of water, PBS, and HA-Apa-Lip@PB-CS-6 NPs to erythrocytes. (D) The morphology changes of erythrocytes incubated with water, PBS, Apa, CS-6, Apa&CS-6, HA-Apa-Lip@PB-CS-6 NPs. Bars represented means ± standard deviation (SD) ($n = 3$). $^{*}P < 0.05$, $^{**}P < 0.01$, and $^{***}P < 0.001$.

each sample treated with HA-Apa-Lip@PB-CS-6 NPs for 4 h remained below 5.0% even at a high concentration of 100 μg/mL (Fig. 3C). Furthermore, no morphological changes were observed in erythrocytes (Fig. 3D). Above results confirmed the biocompatibility of HA-Apa-Lip@PB-CS-6 NPs, which is crucial for their application *in vivo*.

3.4. In vitro cellular uptake and penetration performance of HA-Lip@PB NPs

Considering the high levels of CD44, the HA receptor, on the surface of GC cells, HA can effectively enhance the targeting ability of Lip@PB NPs to tumor cells [28]. By investigating the cellular uptake efficiency of BGC-823 cells to HA-Lip@PB NPs labeling with fluorophore Ce6 (HA-Lip@PB^{Ce6} NPs) *in vitro*, red fluorescence signal reached the peak at 4 h in BGC-823 cells. Furthermore, the red fluorescence intensity was higher than that observed in cells treated with Lip@PB^{Ce6} NPs at each corresponding time point (Figs. 4A and B). Additionally, a competent assay further verified the targeting ability of HA towards BGC-823 cells, as pre-treated BGC-823 cells with HA only exhibited weak red fluorescence around the cell membrane after incubation with HA-Lip@PB^{Ce6} NPs. In contrast, after incubating with solo HA-Lip@PB^{Ce6} NPs, the red fluorescence signals in the cytoplasm of tumor cells increased 70.0%, in comparison to the Lip@PB^{Ce6} NPs group (Figs. 4C and D). In addition, HA modification also enhanced the penetrating ability of HA-Lip@PB^{Ce6} NPs. By using multicellular spheroid as the mimics of real tumor, it was observed that red fluorescence signal in HA-Lip@PB^{Ce6} NPs treated spheroid at the depth's region of ~60 μm was significantly higher than that of free Ce6 treatment at the same region (Figs. 4E and F). In conclusion, the nanodrug delivery system (HA-Lip@PB^{Ce6} NPs) demonstrated high targeting and penetration ability, which is advantageous for tumor therapy *in vivo*.

3.5. In vitro anti-tumor function of HA-Apa-Lip@PB-CS-6 NPs

The MTT assay results revealed that the viability of BGC-823 cells treated with HA-Apa-Lip@PB-CS-6 NPs was significantly lower compared to the Apa&CS-6 treatment group (28.6% vs. 47.9%). Furthermore, the cell viability was much higher in the free drug-treated groups, with 76.2% for Apa and 66.9% for CS-6. These findings clearly demonstrated that HA-Apa-Lip@PB-CS-6 NPs exhibited an enhanced ability to kill cells, as evidenced by a 50.0% increase in cell-killing ability compared to mono-drug treatment (Fig. S5A). Live/dead staining also confirmed the superior effectiveness of HA-Apa-Lip@PB-CS-6 NPs, showing the strongest red fluorescence signal in cells treated with these NPs compared to the other groups (Fig. S5B). These results further supported the conclusion that HA-Apa-Lip@PB-CS-6 NPs had the lowest cell viability among all the treatment groups.

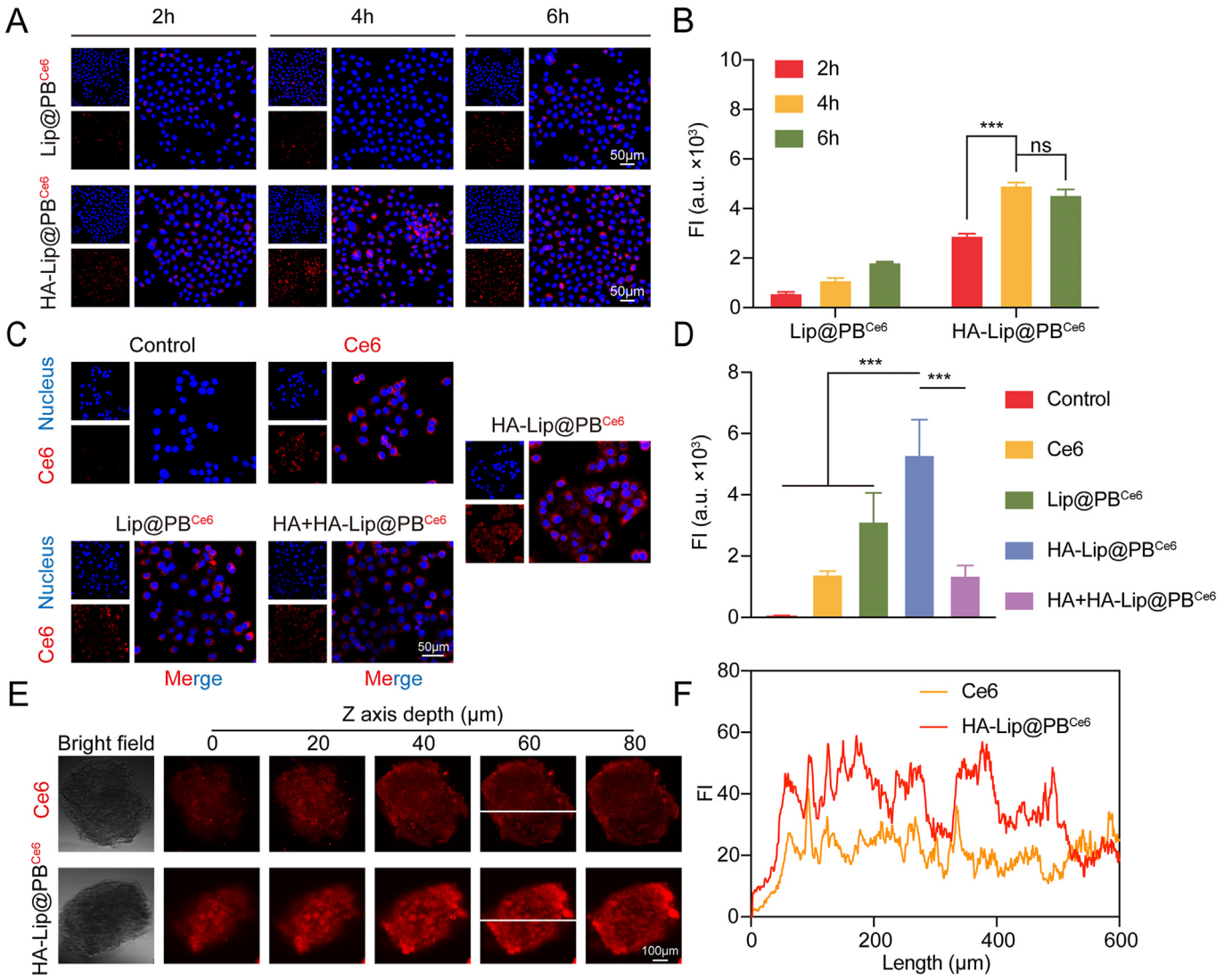

Fig. 4. Cellular uptake and penetration performance of hyaluronan-Lip@Prussian blue nanoparticles (HA-Lip@PB NPs) *in vitro*. (A, B) Fluorescence images of cellular uptake (A) and fluorescence intensity analysis (B) of Lip@PB NPs labeling with fluorophore Ce6 (Lip@PB^{Ce6} NPs) and HA-Lip@PB NPs labeling with fluorophore Ce6 (HA-Lip@PB^{Ce6} NPs) in BGC-823 cells at 2, 4, and 6 h. (C, D) Fluorescence images by confocal laser scanning microscope (CLSM) (C) and fluorescence intensity analysis (D) of BGC-823 cells incubated with free Ce6, Lip@PB^{Ce6}, HA-Lip@PB^{Ce6} and HA + HA-Lip@PB^{Ce6} NPs for 4 h. (E) Fluorescence images of multicellular spheroids, after incubation with free Ce6, and HA-Lip@PB^{Ce6} NPs for 24 h. (F) Mean intensity along the solid white lines in the Z-axis plotted of BGC-823 multicellular spheroids (MCSs). Bars represented means ± standard deviation (SD) ($n = 3$). ***$P < 0.001$, ns: not significant, FI: fluorescence intensity.

Both Apa and CS-6 have been reported to effectively inhibit cell proliferation by disrupting cell cycle [32,39]. Consistent with these findings, flow cytometry analysis (fluorescence-activated cell sorting (FACS) assay) indicated that Apa arrested cell cycle of BGC-823 cells in the G0/G1 phase. On the other hand, formulations containing CS-6 caused cell cycle arrest in the G2/M phase. Interestingly, the HA-Apa-Lip@PB-CS-6 NPs-treated group displayed a significantly higher percentage of cells in the G2/M phase compared to the control group (46.5% vs. 7.2%) (Figs. 5A and B). Additionally, the EdU cell proliferation staining assay showed a high number of cells containing green fluorescence signal in control group, indicating abundant new born cells (Fig. 5C). Compared with relative fluorescence intensity of control group, single drug groups (Apa and CS-6) showed 59.0%–66.9% relative FI, while the values in Apa&CS-6 and HA-Apa-Lip@PB-CS-6 NPs group were 36.0%, and 28.4%, respectively (Fig. 5D). Furthermore, the colon formation assay indicated that HA-Apa-Lip@PB-CS-6 NPs greatly prevented colony formation of BGC-823 cells with 66.8% inhibition rate compared to control group, while the inhibition rate of free drug-treated groups were merely 14.4% for Apa and 25.0% for CS-6 (Figs. 5E and F). Evaluation of cyclin D1, an important regulatory protein in the cell cycle [40], revealed a significant downregulation in HA-Apa-Lip@PB-CS-6 NPs-treated cells (Figs. 5G and S6). Taken together, these results suggested that the inhibitory effect of HA-Apa-Lip@PB-CS-6 NPs on the cyclin D1 should be the primary reason of the anti-tumor function.

3.6. Anti-migration and anti-invasion capability of HA-Apa-Lip@PB-CS-6 NPs in vitro

In previous studies, we have disclosed the anti-metastasis and growth ability of CS-6 in breast cancer [31,36]. Building upon these findings, we sought to investigate whether HA-Apa-Lip@PB-CS-6 NPs could similarly inhibit the growth and distant metastasis of advanced GC [16,17]. By performing wound-healing and transwell assay, we found that free Apa or CS-6 exhibited around 28.6%–

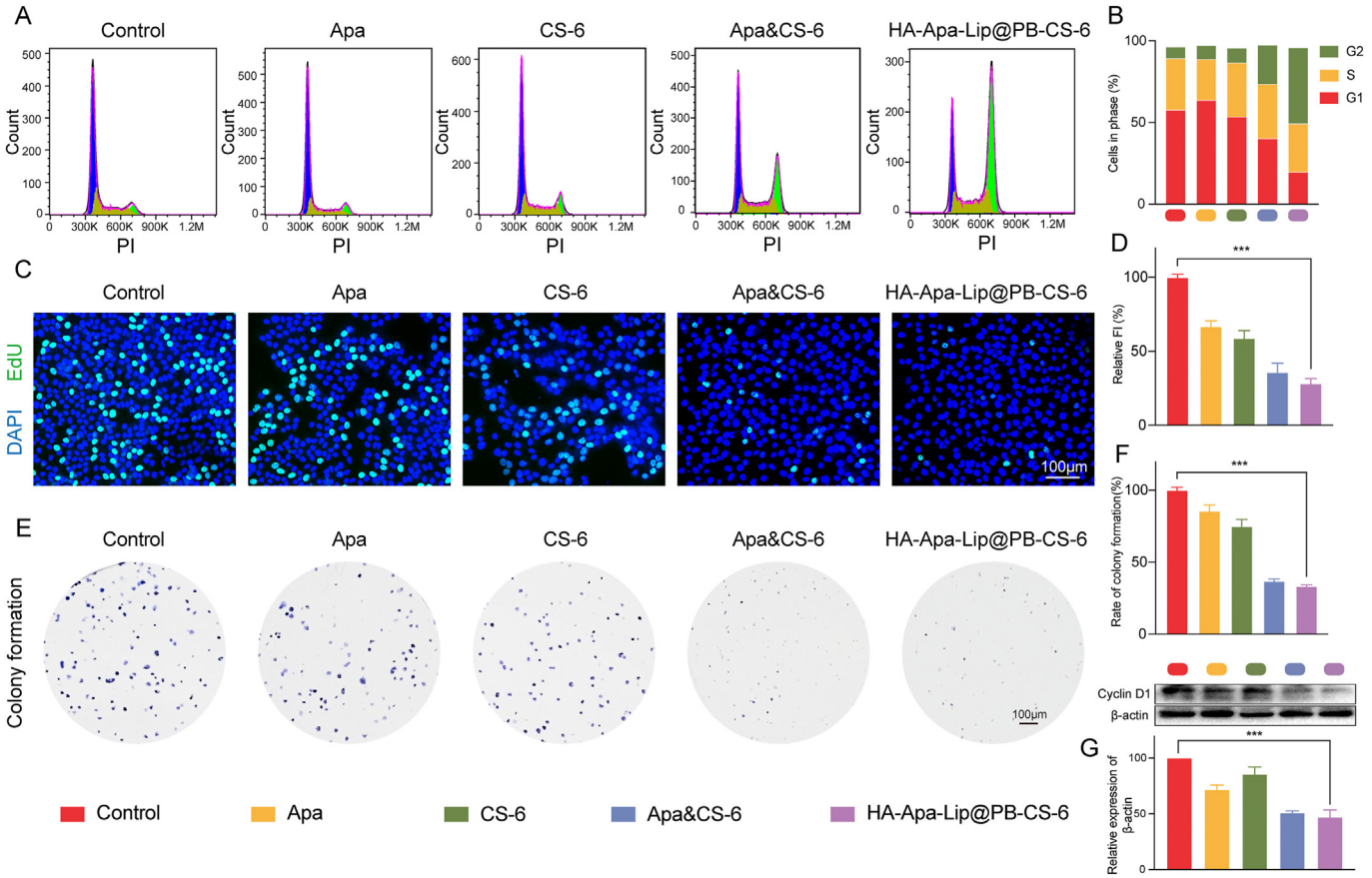

Fig. 5. Anti-gastric cancer (GC) activity and proposed mechanism of hyaluronan-apatinib-Lip@Prussian blue-gamabufotalin nanoparticles (HA-Apa-Lip@PB-CS-6 NPs). (A, B) Cell cycle distribution and analysis of the BGC-823 cells after incubation with various formulations. (C, D) Images of 5-ethynyl-2'-deoxyuridine (EdU) cell proliferation staining by confocal laser scanning microscope (CLSM) (C) and fluorescence intensity (FI) analysis (D). (E, F) Colony formation assay (E) and analysis (F). (G) Western blot of cyclin D1 in BGC-823 cells and quantitative analysis. Bars represented means ± standard deviation (SD) ($n = 3$). ***$P < 0.001$. DAPI: 4',6-diamidino-2-phenylindole; PI: propidium Iodide.

34.4% inhibitory rate, while approximately 54.0% inhibitory rate was found for GC cells treated by Apa&CS-6 and HA-Apa-Lip@PB-CS-6 NPs. Similar trends were found for cell migration and invasion assay (Figs. 6A and B). Furthermore, we investigated the effect of HA-Apa-Lip@PB-CS-6 NPs on the levels of VEGF and MMP-9. Metastasis is associated with the degradation of MMP-9 in the extracellular matrix and basement membrane, as well as the upregulation of VEGF to promote angiogenesis [41]. Western blot assay demonstrated the significant downregulation of HA-Apa-Lip@PB-CS-6 on MMP-9 and VEGF in BGC-823 cells (Figs. 6C and D), the result of which was consistent with our previous reports [32,35]. These results demonstrated that the HA-Apa-Lip@PB-CS-6 NPs inhibited tumor migration at least by means of down-regulating MMP-9 and VEGF.

3.7. Biodistribution and pharmacokinetics of HA-Apa-Lip@PB-CS-6 NPs

Next, the biodistribution and pharmacokinetics of HA-Lip@PB^{Ce6} NPs in BALB/c mice were examined using real-time imaging. As we expected, HA-Lip@PB^{Ce6} NPs gradually accumulated at tumor sites of mice, as indicated by the increase of red fluorescence signal emitted from Ce6 with time extension. The intensity of fluorescence signal, which reached the plateau at 6–12 h after administration, remained in the tumor tissues for up to 48 h. However, Lip@PB^{Ce6} NPs without HA modification exhibited weak fluorescence intensity as well as rapid decline (Figs. 7A and B). Consistent with previous report [23], strong fluorescence signal was found in the livers of mice with HA-Lip@PB^{Ce6} NPs and Lip@PB^{Ce6} NPs treatment, which demonstrated the metabolic route of NPs from liver. Meanwhile, the fluorescence signal in these treated mice gradually decreased over time in the major organs (Figs. 7C and D). Meanwhile, ultra-low fluorescence in the heart of mice with HA-Lip@PB^{Ce6} NPs treatment avoided the toxicity of CS-6 on the cardiocytes, which was the main limitation of sole CS-6 for clinic application [42]. Besides, the fluorescence intensity in tumors with HA-Lip@PB^{Ce6} NPs treatment was consistently higher than that of Lip@PB^{Ce6} NPs treated mice at same point (12, 24 and 48 h) (Figs. 7C and D) due to the targeting performance of HA. Meanwhile, the depth of red fluorescence signal in the tumor section after HA-Lip@PB^{Ce6} NPs treatment was significantly higher than that of Lip@PB^{Ce6} NPs group (Figs. 7E and F). These results demonstrated that the excellent targeting effect of HA-Apa-Lip@PB-CS-6 NPs enabled efficient accumulation and penetration at the tumor site.

After a single intravenous injection of Ce6 and HA-Lip@PB^{Ce6} NPs, blood samples of mice were collected to examine the pharmacokinetics of HA-Apa-Lip@PB-CS-6 NPs *in vivo* by fluorescence imaging. As shown in Fig. 7G, the intensity of fluorescence of blood samples gradually decreased over time, and the half-life of HA-Lip@PB^{Ce6} NPs in the BALB/c mice increased 1.70-fold comparing with that of Ce6 (2.31 h vs. 1.36 h) (Fig. 7H), which showed the function of nanoparticles for extending blood retention time [43].

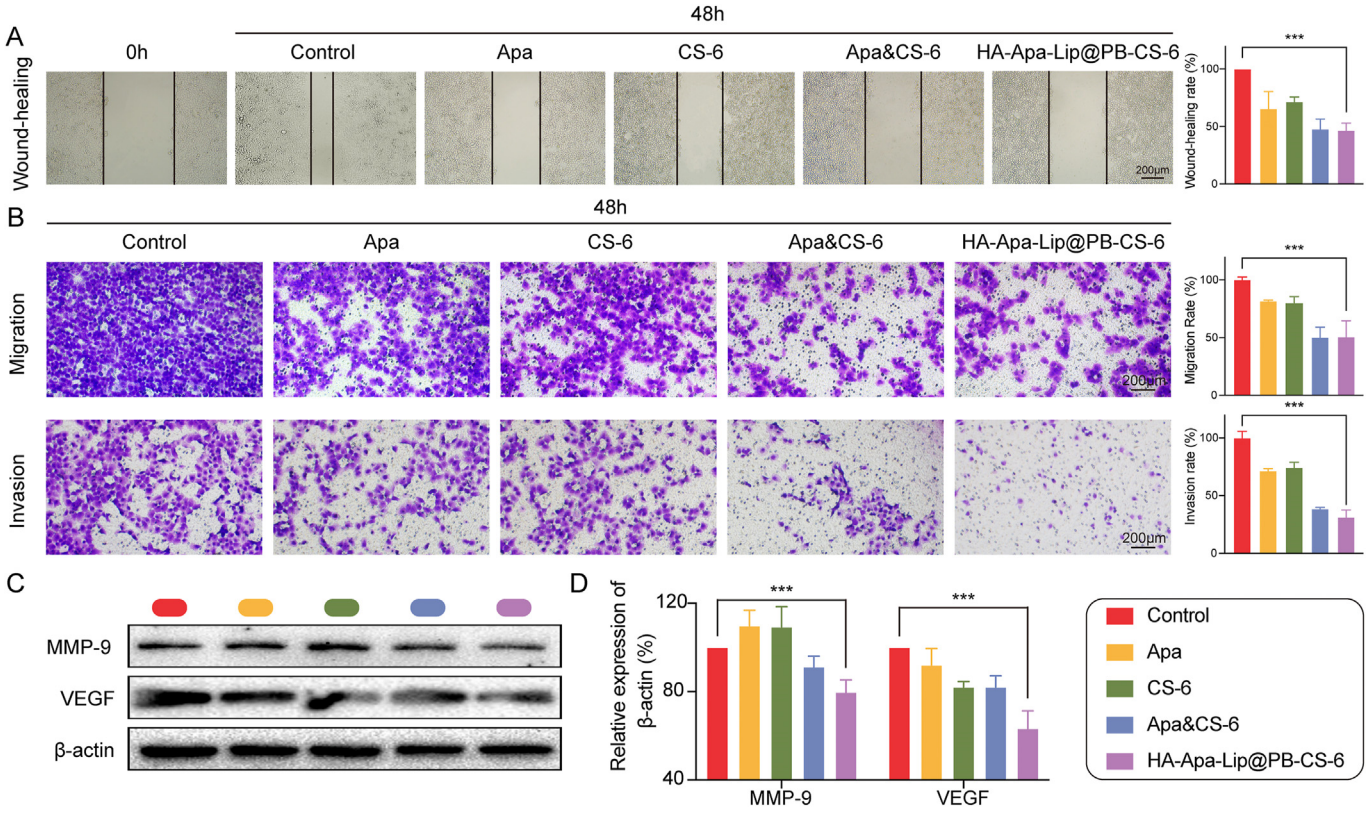

Fig. 6. Anti-metastatic investigation of hyaluronan-apatinib-Lip@Prussian blue-gamabufotalin nanoparticles (HA-Apa-Lip@PB-CS-6 NPs) *in vitro*. (A, B) Wound-healing, migration, and invasion analysis of BGC-823 cells after treated with Apa, CS-6, Apa&CS-6, and HA-Apa-Lip@PB-CS-6 NPs for 48 h (A) and quantitative analysis (B). (C, D) matrix metalloproteinase-9 (MMP-9) and vascular endothelial growth factor (VEGF) expression (C) and quantitative analysis (D) of BGC-823 cells with different treatments. Bars represented means ± standard deviation (SD) ($n = 3$). ***$P < 0.001$.

3.8. Anti-tumor growth and anti-metastasis activity of HA-Apa-Lip@PB-CS-6 NPs in vivo

Encouraged by the efficient tumor cell-killing of HA-Apa-Lip@PB-CS-6 NPs *in vitro*, we therefore performed anti-tumor assay using heterotopic tumor-bearing model according to the treatment schematic diagram (Fig. 8A). Those nude mice were randomly divided into five groups ($n = 5$): PBS, Apa, CS-6, Apa&CS-6, and HA-Apa-Lip@PB-CS-6 NPs. At the end of experiment, the tumor volume of mice with various treatments differentially decreased compared with PBS group (Fig. 8B). The tumor growth inhibiting rate (TIR) in HA-Apa-Lip@PB-CS-6 group reached 67.7%, which was higher than that of Apa&CS-6 treatment group (37.6%), CS-6 group (17.2%), and Apa group (15.7%) (Fig. 8C). Weight records directly indicated that HA-Apa@PB-CS-6 NPs could significantly suppress tumor growth to 0.47 g, while the value in PBS group was 1.61 g (Fig. 8D), and the reliability was supported by the *ex vivo* images of tumor (Figs. 8E and S7). Additionally, H&E staining and terminal deoxynucleotidyl transferase-mediated deoxyuridine triphosphate-nick end labelling (TUNEL) results demonstrated various degrees of tissue necrosis (marked as dotted areas) after different treatments (Apa, CS-6, Apa&CS-6 and HA-Apa-Lip@ PB-CS-6 NPs) (Figs. 8F and S8). In contrast, the PBS group retained intact tumor cell morphology with concentrated nuclei. Furthermore, tumor sections of mice with HA-Apa-Lip@PB-CS-6 NPs treatment exhibited lowest proliferation index compared with other groups, which was supported by Ki67 staining (Fig. 8F). Above results demonstrated the high anti-gastric cancer efficacy of HA-Apa-Lip@PB-CS-6 NPs.

Liver is the frequent site of GC metastasis because of its well vascularized tissue and accessible capillaries [44,45]. Consistent with previous report [46], H&E staining indicated common metastatic nodules in the liver of heterotopic tumor-bearing mice with PBS treatment. However, the nodules in the liver almost disappeared in the HA-Apa-Lip@PB-CS-6 NPs group (Figs. 8G and S9). These results demonstrated that HA-Apa-Lip@PB-CS-6 NPs group can efficiently inhibit tumor metastasis. As tumor metastasis is mainly determined by the levels of MMP-9 and VEGF, we therefore investigated the effect of HA-Apa-Lip@PB-CS-6 NPs on them. Immunofluorescence staining result visually demonstrated the strong inhibition of HA-Apa-Lip@PB-CS-6 NPs on them, compared with PBS treatment group (Fig. 8G). Taken together, these findings suggested that HA-Apa-Lip@PB-CS-6 NPs can inhibit tumor invasion and metastasis through MMP-9/VEGF pathway.

3.9. Biosafety evaluation in vivo

Biosafety evaluation *in vivo* is a crucial factor in assessing the clinical feasibility of nanodrugs [47]. We therefore conducted a comprehensive investigation to evaluate the toxicity of HA-Apa-Lip@PB-CS-6 NPs using various indicators such as complete blood count, hepatic function analysis and renal function analysis, body weight changes, and organ histology. As we expected, HA-Apa-Lip@PB-CS-6 NPs did not change the levels of RBC, platelets (PLT), hemoglobin (HGB), compared with normal mice. Moreover, this kind of treatment significantly reversed inflammatory response in tumor bearing mice to normal condition, which was reflected by the low levels of WBC and normal weight of spleen (Fig. S10) in the

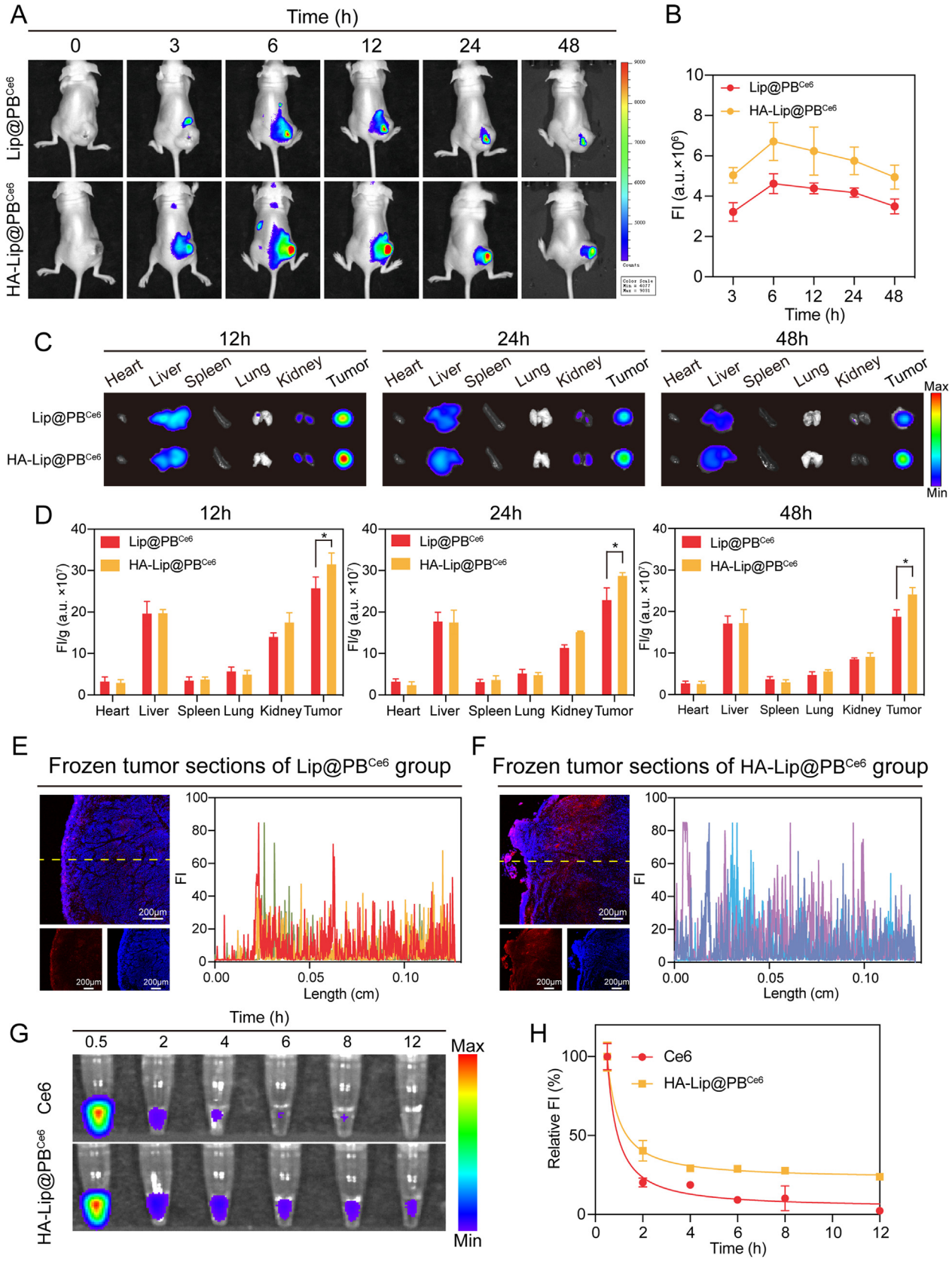

Fig. 7. Biodistribution, intratumor penetration and pharmacokinetic of hyaluronan-Lip@Prussian blue nanoparticles labeling with fluorophore Ce6 (HA-Lip@PB^{Ce6} NPs) *in vivo*. (A, B) Biodistribution of HA-Lip@PB^{Ce6} NPs and Lip@PB^{ce6} NPs in BGC-823 tumor-bearing mice over time measured by the fluorescence (A) and quantitative (B) analysis. (C, D) Fluorescence distribution (C) and quantitative fluorescence analysis (D) of major organs after 12, 24, 48 h post-injection. (E, F) Intratumor penetration ability of Lip@PB^{Ce6} NPs (E) and HA-Lip@PB^{ce6} NPs (F) in frozen tumor sections. Quantitative fluorescence analysis of tumors: the Ce6 fluorescence (red) intensity along the yellow line from tumor surface to tumor core was analyzed by Image J software. (G) Blood fluorescence intensity (FI) of Ce6, HA-Lip@PB^{Ce6} NPs over time. (H) Pharmacokinetic curves of Ce6 and HA-Lip@PB^{Ce6} NPs after different time points. Mean ± standard deviation (SD) ($n = 3$). *$P < 0.05$.

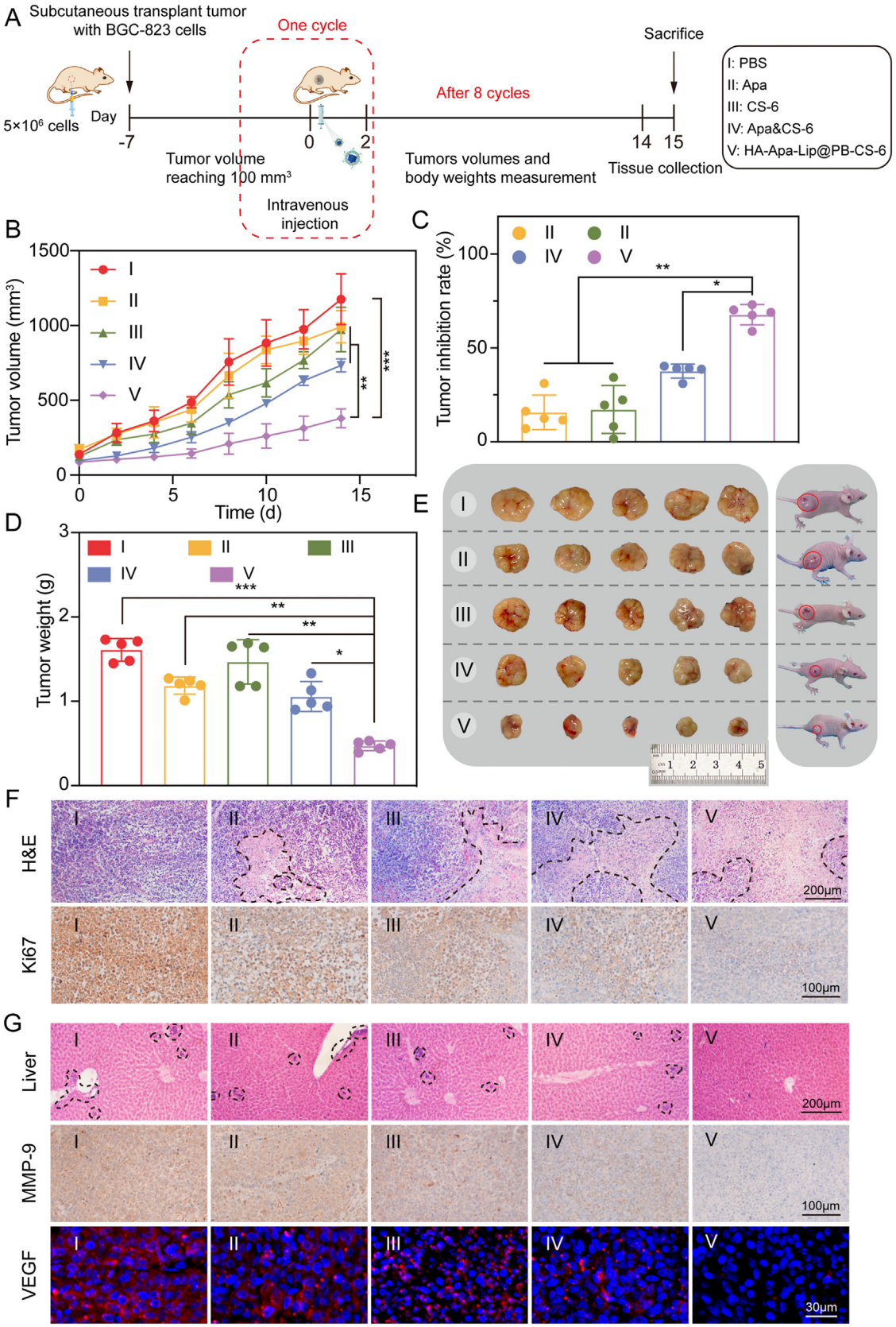

Fig. 8. Treatments of heterotopic gastric cancer (GC) in mice. (A) Schematic illustration of BGC-823 heterotopic gastric tumor implantation and the dosage regimen (I: phosphate buffered saline (PBS) group; II: apatinib (Apa) group; III: CS-6 group; IV: Apa&CS-6 group; V: hyaluronan-apatinib-Lip@Prussian blue-gamabufotalin (HA-Apa-Lip@PB-CS-6) group). (B, C) Tumor volume record (B) and tumor growth inhibiting rate (TIR) (C) of mice with different treatments. (D) The tumor weight of mice after the final treatment in each group. (E) The morphological images of tumors and mice after treatments. (F) Hematoxylin and eosin (H&E) and Ki67 staining of tumor sections with various treatments. (G) Metastatic nodules of liver in each group by H&E staining and immunofluorescent analysis of matrix metalloproteinase-9 (MMP-9) and vascular endothelial growth factor (VEGF) in tumor tissues. Bars represented means ± standard deviation (SD), $n = 5$ per group. $^{*}P < 0.05$, $^{**}P < 0.01$, and $^{***}P < 0.001$.

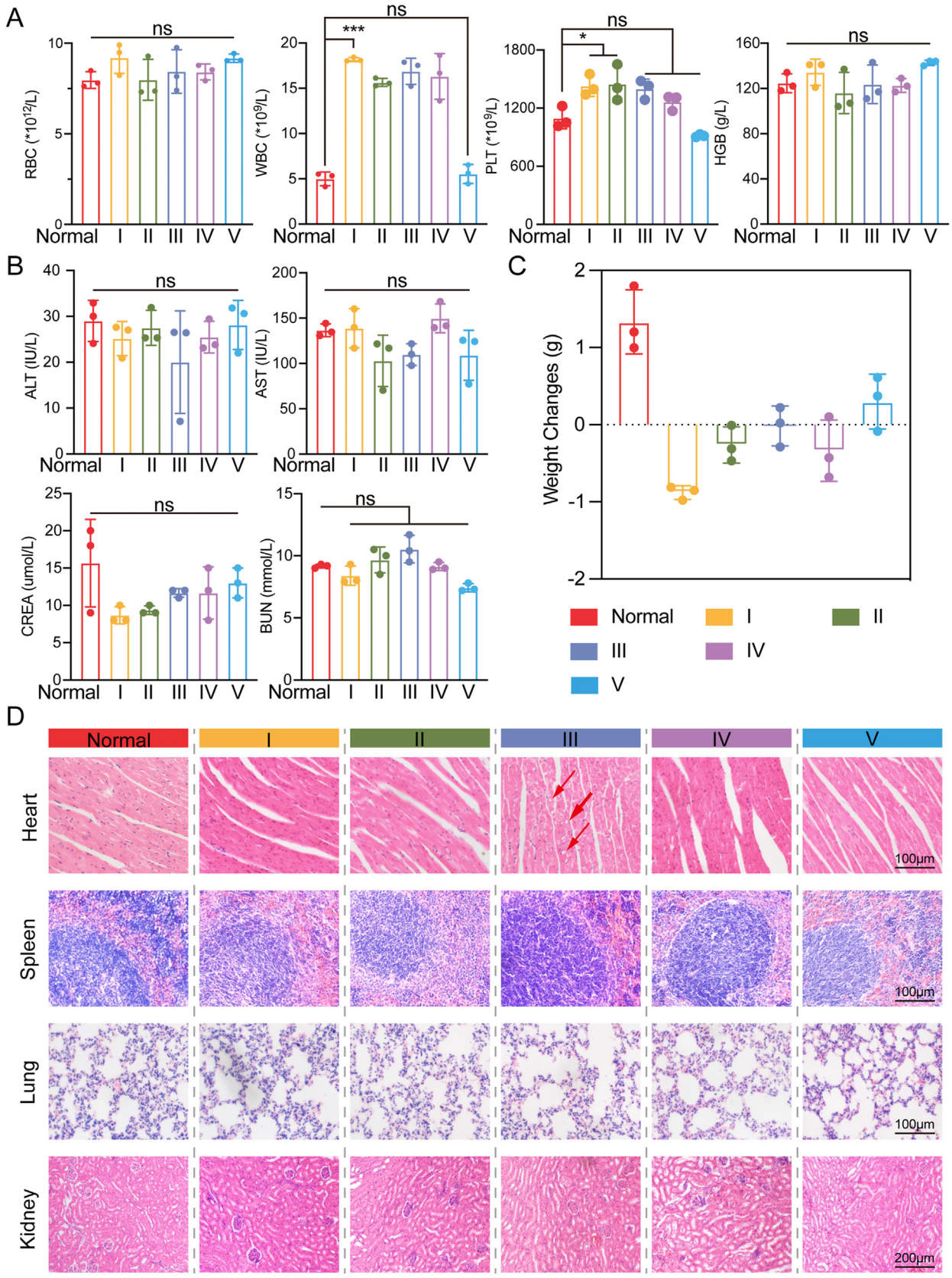

Fig. 9. *In vivo* biosafety evaluation. (A) Complete blood count, including red blood cell (RBC), white blood cell (WBC), platelets (PLT), and hemoglobin (HGB). (B) Blood biochemistry analysis, including liver function indicators: alanine trans-aminase (ALT) and aspartate aminotransferase (AST), and kidney function markers: creatinine (CRE) and blood urea nitrogen (BUN). (C) Changes in relative body weight in different groups during treatments. Weight changes = $m_{day15}-m_{day0}-m_{tumor}$. (m represented mass of mice, m_{tumor} represented mass of tumor). (D) Hematoxylin and eosin (H&E) stained images of major organs in each group. (I: phosphate buffered saline (PBS) group; II: apatinib (Apa) group; III: CS-6 group; IV: Apa&CS-6 group; V: hyaluronan-apatinib-Lip@Prussian blue-gamabufotalin (HA-Apa-Lip@PB-CS-6) group). Bars are means ± SD. *$P < 0.05$, ***$P < 0.001$, ns: not significant.

mice with HA-Apa-Lip@PB-CS-6 NPs treatment (Fig. 9A). Meanwhile, the negligible effect of HA-Apa-Lip@PB-CS-6 NPs on the hepatic/kidney function was supported by the normal levels of various markers including alanine trans-aminase (ALT), aspartate aminotransferase (AST), creatinine (CRE) and blood urea nitrogen (BUN) (Fig. 9B).

In terms of body weight changes, the weight of tumor-bearing mice in PBS treatment group reduced by 4.5% (0.88 g), compared with the weight in the first day. The weight reduced by 1.3% (0.26 g) in Apa treatment group, 0.6% (0.12 g) in CS-6 treatment group, and 1.7% (0.34 g) in Apa&CS-6 treatment group. But weight in HA-Apa-Lip@PB-CS-6 NPs-treated group increased by 1.5% (0.30 g), which indicated the improvement of HA-Apa-Lip@PB-CS-6 NPs with nanoformulation on the toxicity of chemodrugs (Fig. 9C). In addition, the liquefaction necrosis of cardiomyocytes caused by CS-6 (red arrow mark) disappeared in the HA-Apa-Lip@PB-CS-6 NPs group (Fig. 9D). This result demonstrated the great significance for alleviating the cardiotoxicity of CS-6 by constructing nanoformulation. In summary, these results manifested the improvement of nanoparticles on the biosafety of CS-6 and Apa *in vivo*, which is greatly importance for broadening its clinical applications.

4. Conclusions

In conclusion, we have successfully developed an effective strategy for synthesizing HA-modified lipid/PB NPs, which were used for co-delivery of Apa and CS-6. Comparing with free Apa plus/or CS-6, HA-Apa-Lip@PB-CS-6 NPs displayed highly efficient accumulation in tumor sites, controllable drug release, and ultralow cardiocyte toxicity. Additionally, this nano-system with strong penetrating ability into the tumor core regions greatly inhibited tumor growth and metastasis to the liver in heterotopic animal models. Overall, this synergistic chemotherapy strategy demonstrated outstanding anti-tumor efficiency both *in vitro* and *in vivo*, providing an alternative for malignant GC therapy.

CRediT author statement

Binlong Chen, Yanzhong Zhao: Conceptualization, Data curation, Formal analysis, Methodology, Project administration, Writing - Original draft preparation, Reviewing and Editing; **Zichang Lin:** Methodology, Software; **Jiahao Liang, Jialong Fan, Yanyan Huang, Leye He**: Software, Visualization; **Bin Liu**: Resource, Supervision, Validation, Funding acquisition, Writing - Reviewing and Editing.

Declaration of competing interest

The authors declare that there are no conflicts of interest.

Acknowledgments

This work was partially supported by Changsha Municipal Natural Science Foundation (Gramt No.: kq2014265), the Construction Program of Hunan's innovative Province (CN)-High-tech Industry Science and Technology Innovation Leading Project (Project No.: 2020SK2002), the Natural Science Foundation of Hunan Province (Grant No.: 2023JJ40130), Postgraduate Scientific Research Innovation Project of Hunan Province (Project No.: CX20230317), and the Changsha Platform and Talent Plan (kq2203002).

Appendix A. Supplementary data

Supplementary data to this article can be found online at https://doi.org/10.1016/j.jpha.2023.11.011.

References

[1] E.C. Smyth, M. Nilsson, H.I. Grabsch, et al., Gastric cancer, Lancet. 396 (2020) 635–648.
[2] F.M. Johnston, M. Beckman, Updates on management of gastric cancer, Curr. Oncol. Rep. 21 (2019), 67.
[3] N. Charalampakis, P. Economopoulou, I. Kotsantis, et al., Medical management of gastric cancer: A 2017 update, Cancer Med. 7 (2018) 123–133.
[4] Y.Y. Choi, J.H. Cheong, Beyond precision surgery: Molecularly motivated precision care for gastric cancer, Eur. J. Surg. Oncol. 43 (2017) 856–864.
[5] J. Ding, X. Chen, X. Dai, et al., Simultaneous determination of apatinib and its four major metabolites in human plasma using liquid chromatography-tandem mass spectrometry and its application to a pharmacokinetic study, J. Chromatogr. B Analyt. Technol. Biomed. Life Sci. 895–896 (2012) 108–115.
[6] J. Li, X. Zhao, L. Chen, et al., Safety and pharmacokinetics of novel selective vascular endothelial growth factor receptor-2 inhibitor YN968D1 in patients with advanced malignancies, BMC Cancer. 10 (2010), 529.
[7] S. Tian, H. Quan, C. Xie, et al., YN968D1 is a novel and selective inhibitor of vascular endothelial growth factor receptor-2 tyrosine kinase with potent activity *in vitro* and *in vivo*, Cancer Sci. 102 (2011) 1374–1380.
[8] R. Geng, L. Song, J. Li, et al., The safety of apatinib for the treatment of gastric cancer, Expet Opin. Drug Saf. 17 (2018) 1145–1150.
[9] G. Roviello, A. Ravelli, K. Polom, et al., Apatinib: A novel receptor tyrosine kinase inhibitor for the treatment of gastric cancer, Cancer Lett. 372 (2016) 187–191.
[10] J. Ding, X. Chen, Z. Gao, et al., Metabolism and pharmacokinetics of novel selective vascular endothelial growth factor receptor-2 inhibitor apatinib in humans, Drug Metab. Dispos. 41 (2013) 1195–1210.
[11] J.A. Ajani, T.A. D'Amico, D.J. Bentrem, et al., Gastric cancer, version 2.2022, NCCN clinical practice guidelines in oncology, J. Natl. Compr. Cancer Netw. 20 (2022) 167–192.
[12] N. Tang, L. Shi, Z. Yu, et al., Gamabufotalin, a major derivative of bufadienolide, inhibits VEGF-induced angiogenesis by suppressing VEGFR-2 signaling pathway, Oncotarget. 7 (2016) 3533–3547.
[13] Y.B.L. Moreno, A. Katz, W. Miklos, et al., Hellebrin and its aglycone form hellebrigenin display similar in vitro growth inhibitory effects in cancer cells and binding profiles to the alpha subunits of the Na+/K+-ATPase, Mol. Cancer. 12 (2013), 33.
[14] J. Fan, B. Liu, Y. Long, et al., Sequentially-targeted biomimetic nano drug system for triple-negative breast cancer ablation and lung metastasis inhibition, Acta Biomater. 113 (2020) 554–569.
[15] B. Yuan, R. Shimada, K. Xu, et al., Multiple cytotoxic effects of gamabufotalin against human glioblastoma cell line U-87, Chem. Biol. Interact. 314 (2019), 108849.
[16] S. Nagini, Carcinoma of the stomach: A review of epidemiology, pathogenesis, molecular genetics and chemoprevention, World J. Gastrointest. Oncol. 4 (2012) 156–169.
[17] H. Wong, T. Yau, Targeted therapy in the management of advanced gastric cancer: Are we making progress in the era of personalized medicine? Oncologist. 17 (2012) 346–358.
[18] Y. Ke, J. Zhu, Y. Chu, et al., Bifunctional fusion membrane-based hydrogel enhances antitumor potency of autologous cancer vaccines by activating dendritic cells, Adv. Funct. Mater. 32 (2022), 2201306.
[19] Q. Liu, D. Zhang, H. Qian, et al., Superior antitumor efficacy of IFN-alpha2b-incorporated photo-cross-linked hydrogels combined with T cell transfer and low-dose irradiation against gastric cancer, Int. J. Nanomed. 15 (2020) 3669–3680.
[20] D. Zhang, Y. Chu, H. Qian, et al., Antitumor activity of thermosensitive hydrogels packaging gambogic acid nanoparticles and tumor-penetrating peptide iRGD against gastric cancer, Int. J. Nanomed. 15 (2020) 735–747.
[21] W. Chen, K. Shi, J. Liu, et al., Sustained co-delivery of 5-fluorouracil and cisplatinum via biodegradable thermo-sensitive hydrogel for intraoperative synergistic combination chemotherapy of gastric cancer, Bioact. Mater. 23 (2023) 1–15.
[22] X. Cai, W. Gao, M. Ma, et al., A prussian blue-based core-shell hollow-structured mesoporous nanoparticle as a smart theranostic agent with ultrahigh pH-responsive longitudinal relaxivity, Adv. Mater. 27 (2015) 6382–6389.
[23] J. Liang, C. Wang, J. Fan, et al., Hybrid membrane-camouflaged hollow prussian blue nanoparticles for shikonin loading and combined chemo/photothermal therapy of metastatic TNBC, Materials Today Advances. 14 (2022), 100245.
[24] C. Tong, X. Zhong, Y. Yang, et al., PB@PDA@Ag nanosystem for synergistically eradicating MRSA and accelerating diabetic wound healing assisted with laser irradiation, Biomaterials. 243 (2020), 119936.
[25] B. Liu, W. Wang, J. Fan, et al., RBC membrane camouflaged prussian blue nanoparticles for gamabutolin loading and combined chemo/photothermal therapy of breast cancer, Biomaterials. 217 (2019), 119301.
[26] C. Xiao, C. Tong, J. Fan, et al., Biomimetic nanoparticles loading with gamabutolin-indomethacin for chemo/photothermal therapy of cervical cancer and anti-inflammation, J. Contr. Release. 339 (2021) 259–273.
[27] E. Sackmann, Supported membranes: scientific and practical applications, Science. 271 (1996) 43–48.
[28] R.H. Tammi, A. Kultti, V.M. Kosma, et al., Hyaluronan in human tumors: pathobiological and prognostic messages from cell-associated and stromal hyaluronan, Semin. Cancer Biol. 18 (2008) 288–295.

[29] A. Ianevski, A.K. Giri, T. Aittokallio, SynergyFinder 2.0: visual analytics of multi-drug combination synergies, Nucleic Acids Res. 48 (2020) W488–W493.
[30] H. Meng, M. Wang, H. Liu, et al., Use of a lipid-coated mesoporous silica nanoparticle platform for synergistic gemcitabine and paclitaxel delivery to human pancreatic cancer in mice, ACS Nano. 9 (2015) 3540–3557.
[31] H. Zhou, P. You, H. Liu, et al., Artemisinin and Procyanidins loaded multi-functional nanocomplexes alleviate atherosclerosis via simultaneously modulating lipid influx and cholesterol efflux, J. Contr. Release. 341 (2022) 828–843.
[32] Y. Long, Z. Wang, J. Fan, et al., A hybrid membrane coating nanodrug system against gastric cancer via the VEGFR2/STAT3 signaling pathway, J. Mater. Chem. B 9 (2021) 3838–3855.
[33] Q. Xie, B. Li, J. Fan, et al., Biomimetic hybrid-cell membrane nanoparticles loaded with panaxytriol for breast cancer combinational therapy, Mater. Des. 223 (2022), 111219.
[34] Z. Lei, J. Fan, X. Li, et al., Biomimetic graphene oxide quantum dots nanoparticles targeted photothermal-chemotherapy for gastric cancer, J. Drug Target. 31 (2023) 320–333.
[35] J. Fan, Y. Qin, C. Xiao, et al., Biomimetic PLGA-based nanocomplexes for improved tumor penetration to enhance chemo-photodynamic therapy against metastasis of TNBC, Materials Today Advances. 16 (2022), 100289.
[36] J.R. Casey, S. Grinstein, J. Orlowski, Sensors and regulators of intracellular pH, Nat. Rev. Mol. Cell Biol. 11 (2010) 50–61.
[37] G. Liu, X. Zhao, Y. Zhang, et al., Engineering biomimetic platesomes for pH-responsive drug delivery and enhanced antitumor activity, Adv. Mater. 31 (2019), 1900795.
[38] T.M. Allen, P.R. Cullis, Liposomal drug delivery systems: from concept to clinical applications, Adv. Drug Deliv. Rev. 65 (2013) 36–48.
[39] L.J. Deng, Y. Li, M. Qi, et al., Molecular mechanisms of bufadienolides and their novel strategies for cancer treatment, Eur. J. Pharmacol. 887 (2020), 173379.
[40] W. Müller, T. Noguchi, H.C. Wirtz, et al., Expression of cell-cycle regulatory proteins cyclin D1, cyclin E, and their inhibitor p21 WAF1/CIP1 in gastric cancer, J. Pathol. 189 (1999) 186–193.
[41] A. Dongre, R.A. Weinberg, New insights into the mechanisms of epithelial-mesenchymal transition and implications for cancer, Nat. Rev. Mol. Cell Biol. 20 (2019) 69–84.
[42] Z. Yu, W. Guo, X. Ma, et al., Gamabufotalin, a bufadienolide compound from toad venom, suppresses COX-2 expression through targeting IKKβ/NF-κB signaling pathway in lung cancer cells, Mol. Cancer. 13 (2014), 203.
[43] Q. Zhang, C. Deng, Y. Fu, et al., Repeated administration of hyaluronic acid coated liposomes with improved pharmacokinetics and reduced immune response, Mol. Pharm. 13 (2016) 1800–1808.
[44] A. Schroeder, D.A. Heller, M.M. Winslow, et al., Treating metastatic cancer with nanotechnology, Nat. Rev. Cancer. 12 (2011) 39–50.
[45] D.X. Nguyen, P.D. Bos, J. Massagué, Metastasis: from dissemination to organ-specific colonization, Nat. Rev. Cancer. 9 (2009) 274–284.
[46] Z. Zhang, B. Niu, J. Chen, et al., The use of lipid-coated nanodiamond to improve bioavailability and efficacy of sorafenib in resisting metastasis of gastric cancer, Biomaterials. 35 (2014) 4565–4572.
[47] J. Wolfram, M. Zhu, Y. Yang, et al., Safety of nanoparticles in medicine, Curr. Drug Targets. 16 (2015) 1671–1681.